INL/JOU-23-71003-Revision-0

SPH modeling of biomass granular flow: Theoretical implementation and experimental validation

August 2023

Yumeng Zhao, Jordan Lee Klinger, David C. Dayton, Sheng Dai, Wencheng Jin

INL/JOU-23-71003-Revision-0

SPH modeling of biomass granular flow: Theoretical implementation and experimental validation

Yumeng Zhao, Jordan Lee Klinger, David C. Dayton, Sheng Dai, Wencheng Jin

August 2023

Idaho National Laboratory
Idaho Falls, Idaho 83415

http://www.inl.gov

Prepared for the
U.S. Department of Energy
Under DOE Idaho Operations Office
Contract DE-AC07-05ID14517

SPH modeling of biomass granular flow: theoretical implementation and experimental validation

Yumeng Zhao[a,b], Wencheng Jin[a,*], Jordan Klinger[a], David C. Dayton[c], Sheng Dai[b]

[a]*Energy and Environment Science and Technology Directorate, Idaho National Laboratory, USA*
[b]*School of Civil and Environmental Engineering, Georgia Institute of Technology, USA*
[c]*Technology Advancement & Commercialization, RTI International, USA*

Abstract

The commercialization of biomass-derived energy is impeded by flowability challenges arising from the feeding and handling of granular biomass materials in full-scale biorefineries. To overcome these obstacles, a robust and accurate model to simulate the flow of granular biomass is indispensable. However, conventional mesh-based numerical codes are limited by inherent mesh distortion in simulating large deformation that commonly occurs in granular biomass handling. In this study, we propose a graphics processing unit (GPU)-accelerated meshless Smoothed Particle Hydrodynamics (SPH) code to model the flow of granular biomass materials. A modified void ratio-based mass conversation, a hybrid particle-to-particle/surface frictional boundary treatment, and a hypoplastic constitutive model are implemented. Four numerical examples, an elastic block sliding on inclined planes, sand column collapse, Angle of Repose, and axial compression tests for pine chips, were simulated using the developed SPH code. The results demonstrate good agreement between numerical predictions and analytical and experimental data for all four examples, validating the SPH code and increasing confidence that it can be applied to simulate more complex granular biomass handling processes, such as hopper feeding or auger conveyance.

Keywords: SPH, Granular Flow Modeling, Granular Biomass Materials, Angle of Repose, Axial Compression

---

[*] Corresponding author
Email address: `Wencheng.Jin@inl.gov` (Wencheng Jin)

Preprint submitted to Powder Technology *July 11, 2023*

1. Introduction

Biomass is an environmentally sustainable energy resource with the potential to displace fossil fuels and reduce greenhouse gas emissions. Direct combustion of biomass is considered a carbon-neutral energy process, as long as the CO_2 released through burning has been recently captured from the atmosphere [1, 2, 3, 4]. Additionally, biomass can be converted into biofuels (e.g., ethanol) or sustainable biochemicals (e.g., succinic acid) through biochemical or thermochemical process [5, 6, 7]. The U.S. Department of Energy (DOE) estimates that about 1.2 billion tons of biomass feedstock can be sustainably produced on an annual basis by 2040, which can be converted into 90-108 billion gallons of biofuels and replace more than 30% of the U.S. petroleum consumption based on the 2005 consumption level [8]. However, biomass-derived energy accounts for less than 5% in U.S. energy consumption according to the U.S. Energy Information Administration [9].

Expanding the bioenergy sector poses a significant challenge due to the handling difficulties associated with feedstock throughout the successive process of harvesting, pretreatment, storage, transport, and feeding [10]. Successful and uninterrupted operation of these handling processes directly relies on the flow performance of granular biomass [11], which unfortunately are poor [12] due to irregular shapes, high interlocking and friction, high compressibility, low density, fibrous nature and sensitivity to moisture content. These properties contrast with conventional granular materials (e.g., sands) that have been extensively studies. The poor flowability of biomass manifests as arching, bridging, and jamming in various handling equipment [12, 13, 14, 15, 16, 17]. Conducting economically viable experimental investigations to address these issues is challenging due to the variability of biomass feedstock and the size limitation of handling equipment. Furthermore, handling issues are scale-dependent, and knowledge obtained from small-scale experiments may not be transferrable to address problems at a large scale. Therefore, physical-based numerical modeling, which is scale independent, is greatly needed to address these handling issues.

Over the last decade, a variety of computational methods have been used to simulate the flow of granular materials, including biomass. However, traditional mesh-based continuum methods such as the Finite Element Method (FEM), Finite Volume Method (FVM), and Finite Difference Method (FDM) have limitations due to mesh distortion caused by large material deformation. To address this, several improvements have been proposed, such as the Coupled Eulerian Lagrangian FEM (CEL-FEM) and Material Point Method (MPM) solve Lagrangian-based material particles with the aid of Eulerian-based background grids [18, 19], the Particle Finite Element Method (PFEM) treats finite element nodes as particles and constructs a new mesh at each time step[20], the Arbitrary-Lagrangian-Eulerian (ALE) method uses both the Lagrangian and Eulerian description of a domain and allow the mesh to move arbitrarily from the constraint of Lagrangian or Eulerian nodes [21, 22]. While these improvements have been successful in simulating flow in handling equipment with simple geometry [23, 24], they are still unable to model granular material flow and transport in handling equipment with complex geometry, such as an auger. In parallel, some studies have used Discrete Element Method (DEM) to study granular flow for its inherent Lagrangian description and meshless characteristic [25, 26, 27]. DEM is capable of capturing particle-level mechanical interactions and modeling particles with different shapes and fabrics. However, nonphysical material parameterization for the contact model at the micro-scale and excessively high computational cost [28, 29] makes DEM impractical for modeling granular flow at the industry scale, especially when particle-level mechanisms are not of interest.

Smoothed Particle Hydrodynamics (SPH) is a meshless method that does not require a background grid, making it particularly useful for simulating large deformation and large-scale phenomena with no interface tracking. SPH was originally introduced to model astrophysics phenomena [30, 31] and has been successfully applied to model fluids [32, 33, 34]. In recent years, SPH has been extended to model solids and granular materials, with significant improvements in constitutive models, boundary treatments, and numerical techniques. For instance, elasto-plastic [35, 36, 37], hypoplastic [38, 39] and rheological models [38] were successfully implemented in the SPH framework. Additionally, proposed particle-based [40, 41, 42, 43], surface-based [44], or combined boundary [45] conditions are compatible with granular flow systems. Special numerical techniques have also been developed to solve challenging numerical issues of granular flow, including boundary penetration [41], frictional wall [44, 46, 47, 45], and numerical instability [37, 39, 42, 43]. Efforts have also been made to couple granular soil with fluid [35] or structure [40, 48, 43]. All these applications support SPH as a promising method for modeling granular materials for large-scale practical problems. Despite its promise, to our knowledge, SPH has not yet been widely applied to model granular biomass materials to address flow challenges.

This study developed an SPH code for modeling granular biomass flow by modifying DualSPHysics, an open-source code initially developed for simulating fluid mechanics problems [49]. To do so, the mass conservation was initially reformulated in terms of void ratio. Then, the mathematical formulation of frictional, no-slip, and free-slip boundary conditions was developed following Wang et al. [44] and Zhan et al. [45]. Finally, these modifications were adapted in a Gudehus-Bauer (G-B) hypoplastic model [50, 51] for granular material mechanical behavior modeling. The modified SPH tool was validated through several simulation benchmark examples, including an elastic block sliding along an inclined and frictional plane to validate the boundary treatments, a series of sand collapse tests to validate the G-B hypoplastic model, and a set of Angle of Repose (AoR) tests and axial compression tests for milled loblolly pine to demonstrate the ability to accurately model granular biomass flow. This study lays the foundation for accurately modeling biomass granular material flow in various handling equipment (e.g., hopper, screw, conveyor) using the SPH method in a validated G-B hypoplastic model.

2. Theory

2.1. SPH overview

The theory of SPH comes from a mathematical identity for a function $f(\boldsymbol{x})$ in a domain Ω:

$$f(\boldsymbol{x}) = \int_{\Omega} f(\boldsymbol{x}')\delta(\boldsymbol{x} - \boldsymbol{x}')d\boldsymbol{x}' \tag{1}$$

where f is a function of the position vector $\boldsymbol{x}$, and $\delta(\boldsymbol{x}-\boldsymbol{x}')$ is the Dirac delta function:

$$\delta(\boldsymbol{x}-\boldsymbol{x}') = \begin{cases} 1, & \boldsymbol{x}=\boldsymbol{x}' \\ 0, & \boldsymbol{x}\neq\boldsymbol{x}' \end{cases} \tag{2}$$

In order to solve complex differential equations numerically, SPH made two approximations. First, Eq.1 is rewritten as:

$$< f(\boldsymbol{x}) >= \int_{\Omega} f(\boldsymbol{x}')W(\boldsymbol{x}-\boldsymbol{x}', h)d\boldsymbol{x}' \tag{3}$$

where W is a kernel function that satisfies the normalization condition, delta function property, and compact condition [52]. $< \cdot >$ is a standard notation for kernel approximation in SPH. The second approximation is to discretize the continuous domain into discrete mass points and thus convert volume integral in Eq. 3 into summation as:

$$f(\boldsymbol{x}_a) = \sum_b f(\boldsymbol{x}_b)\frac{m_b}{\rho_b}W_{ab} \tag{4}$$

in which $\boldsymbol{x}_b$ is the position vector of a mass particle b that is within the kernel distance h of $\boldsymbol{x}_a$, m_b and ρ_b are its particle mass and density. $W_{ab} = W(\boldsymbol{x}_a - \boldsymbol{x}_b, h)$ vanishes if $||\boldsymbol{x}_a - \boldsymbol{x}_b > h||$. Similarily, the gradient of $f(\boldsymbol{x})$ can be approximated as:

$$\boldsymbol{\nabla} f(\boldsymbol{x}_a) = \sum_b f(\boldsymbol{x}_b)\frac{m_b}{\rho_b}\boldsymbol{\nabla}_a W_{ab} \tag{5}$$

2.2. Discretization of governing equations

For each SPH material point, the governing equations of mass and momentum conservation are:

$$\frac{d\rho}{dt} + \rho\boldsymbol{\nabla}\cdot\boldsymbol{v} = 0, \tag{6}$$

$$\frac{d\boldsymbol{v}}{dt} = \frac{\boldsymbol{\nabla}\cdot\boldsymbol{\sigma}}{\rho} + \boldsymbol{g} + \boldsymbol{f}^{ext}. \tag{7}$$

Here ρ, $\boldsymbol{v}$ and $\boldsymbol{\sigma}$ are the bulk density, velocity, and stress tensor at a material point, $\boldsymbol{g}$ denotes the gravitational acceleration, and $\boldsymbol{f}^{ext}$ represents the applied external forces. Note in Eq. 6 the material derivative $d(\cdot)/dt$ formulation is used since the derivation of SPH governing equations is in a Lagrangian form.

As reviewed by Jin et al. [28], the critical state theory-based constitutive models are one of the most promising models for capturing the complex mechanical behavior of granular biomass materials. These models use the void ratio as an independent variable to track the material state, in addition to the stress tensor. Thus, we rewrite the conservation of mass equation Eq.6 in a more convenient void ratio formulation. Recall the void ratio e, bulk density ρ, and solid density ρ_s have the following relationship:

$$\rho = \rho_s/(1+e) \tag{8}$$

Given that the solid density ρ_s is a constant, we can associate Eqs. 6 and 8 together as:

$$\frac{d(1/(1+e))}{dt} + \frac{1}{(1+e)}\nabla \cdot \boldsymbol{v} = 0 \tag{9}$$

Rewrite Eq. 9, we obtain the void ratio evolution based on the conservation of mass in Eq. 6 as:

$$-\frac{de}{dt} + (1+e)\nabla \cdot \boldsymbol{v} = 0 \tag{10}$$

To discretize the governing equations in SPH formulation, we first discretize the velocity gradient by applying Eq. 5 as:

$$\nabla \boldsymbol{v}_a = \sum_{b \in s} m_b \boldsymbol{v}_{ab} \frac{1}{\rho_b} \cdot \nabla_a W_{ab} \tag{11}$$

here $\boldsymbol{v}_{ab} = \boldsymbol{v}_a - \boldsymbol{v}_b$, $b \in s$ means particle b is within the kernel influence zone (excluding the boundary particles) of the material particle a. The strain rate tensor $\dot{\boldsymbol{\epsilon}}$ can be expressed as:

$$\dot{\boldsymbol{\epsilon}} = 1/2\Big(\nabla \boldsymbol{v} + (\nabla \boldsymbol{v})^T\Big) \tag{12}$$

The divergence of velocity $\nabla \cdot \boldsymbol{v}$ is thus the trace of the strain rate tensor as:

$$\nabla \cdot \boldsymbol{v} = D_{kk} \tag{13}$$

Eqs. 10-13 can then be used to solve the mass conservation equation in the SPH formulation. For the conservation of momentum, Eq. 7 is written as:

$$\frac{d\boldsymbol{v}_a}{dt} = \sum_{b\in s} m_b\Big(\frac{\boldsymbol{\sigma}_a}{\rho_a^2} + \frac{\boldsymbol{\sigma}_b}{\rho_b^2}\Big)\cdot\nabla_a W_{ab} + \boldsymbol{g}_a + \frac{\boldsymbol{f}_{w\to a}}{m_a} + \sum_{b\in s} m_b \Pi_{ab}\cdot\nabla_a W_{ab} \tag{14}$$

in which the first term on the right-hand side is derived with the following considerations:

$$\frac{\boldsymbol{\nabla}\cdot\boldsymbol{\sigma}}{\rho}|_a = \Big[\frac{\boldsymbol{\sigma}}{\rho^2}\boldsymbol{\nabla}\cdot\rho + \boldsymbol{\nabla}\cdot\Big(\frac{\boldsymbol{\sigma}}{\rho}\Big)\Big]_a \approx \sum_{b\in s} m_b\Big(\frac{\boldsymbol{\sigma}_a}{\rho_a^2} + \frac{\boldsymbol{\sigma}_b}{\rho_b^2}\Big)\cdot\nabla_a W_{ab} \tag{15}$$

$\boldsymbol{g}_a$ and $\boldsymbol{f}_{w\to a}$ in Eq. 14 denote the gravitational force and the boundary force from the wall applied to the material particle a, respectively. The formulation of the boundary force term will be detailed in Section 2.4. The last term in Eq. 14 is an artificial viscosity term used to stabilize the numerical simulation and prevent large unphysical oscillations [39, 36]. In which Π_{ab} is expressed as [53]:

$$\Pi_{ab} = \begin{cases} -\frac{\alpha_\mu c_s h}{\bar{\rho}_{ab}}\frac{\boldsymbol{v}_{ab}\cdot\boldsymbol{x}_{ab}}{\boldsymbol{x}_{ab}^2 + 0.01h^2}, & \text{if } \boldsymbol{v}_{ab}\cdot\boldsymbol{x}_{ab} < 0 \\ 0, & \text{otherwise} \end{cases} \tag{16}$$

where α_μ is the coefficient of artificial viscosity, c_s is the speed of sound, h is the kernel radius, $\bar{\rho}_{ab}$ and $\boldsymbol{x}_{ab}$ denote the average density of the material particles a and b and the distance between them.

2.3. Smoothing kernel

The stability of SPH simulation is known to be affected by the selection of the kernel function. An improper kernel function can result in so-called pairing instability that manifests as particle clumps formation during simulation. According to Dehnen and Aly [54], this occurs when an SPH smoothing kernel has a negative Fourier transform for some wave vector and a sufficient amount of neighboring particles are included in this kernel. To avoid this pairing instability, we select the Wendland C^2 kernel [55, 54, 49] expressed as

$$W(r,h) = \frac{21}{16\pi h^3}\Big(1 - \frac{r}{2h}\Big)^4\Big(\frac{2r}{h} + 1\Big), 0 \leq \frac{r}{h} \leq 2 \tag{17}$$

In addition, the Wendland C^2 kernel function is able to tolerate more neighboring particles within a kernel without causing a significant numerical error, thus, is a good candidate for problems with highly disordered particles [54, 56]. However, care needs to be taken as this kernel can produce comparably large errors when there is a low number of neighboring particles [54, 56].

Another well-known instability in SPH is called tensile instability, which can also contribute to particle clump formation. This instability arises from the attractive force between two particles when their stresses are negative. For non-cohesive granular materials, tensile stress (i.e., attractive forces between particles) does not physically exist and the tensile instability will not occur as demonstrated by Bui et al. [35, 40]. To avoid unphysical tensile stress generated in this explicit SPH scheme, we numerically limit the maximum value of stress components by using σ_{ii} = -10 Pa, $\sigma_{ij/ik} = 0$ if $\sigma_{ii} > 0$, where i, j, k refers to the coordinate directions. A more rigorous treatment is to adjust for stresses in principal directions [47] . However, the proposed alternative method shows no tensile instability from our simulations and is adopted in this paper. More sophisticated numerical treatments to mitigate tensile instability, such as the artificial stress method [53], will be implemented for modeling cohesive granular materials.

2.4. Boundary treatment - frictional boundary conditions

A proper boundary treatment is one of the key aspects for an SPH code, and several numerical techniques have been proposed to enforce suitable boundary conditions for granular materials. Among them, the dummy particle method, which uses a few layers of particles to represent the walls is the most common one. This method guarantees full kernel support for all material particles, which renders the material state update and the no-slip boundary condition implementation straightforward. However, accurately extrapolating the stress and velocity of dummy boundary particles from the state of the material particles, which ensures no penetration and smooth stress distributions across boundaries, is a challenging task [36, 40, 41, 38, 37, 39, 48, 43]. The ghost particle method, which mirrors any material particles close to a boundary with a certain distance and uses those ghost particles to provide support for SPH calculation, is another boundary handling technique and is usually used to enforce free-slip boundary condition [36, 41]. A combination of dummy and ghost particle methods is called modified dynamic boundary condition (mdbc) and has been adopted to capture mixed boundary conditions [57, 42, 58]. All the above methods are based on particle-to-particle interaction, which hinders them from enforcing the frictional boundary condition. Some attempts are made to take friction into account using the particle-to-particle method with mixed success [47]. However, the particle-to-surface approach is more suitable for frictional boundary realization. This method needs a predefined boundary surface, the interaction of material particles with respect to the boundary is achieved through either a partial penetration or a momentum method [35, 44, 46]. To preserve the benefits of both the particle-to-particle and particle-to-surface contacts, Zhan et al. [45] proposed a hybrid contact approach to realize all boundary conditions. The idea of this method is to push back the material particle with external force when it moves toward a wall particle and the distance between the two particles is less than an allowed value. Boundary particles do not involve the state variable updating but only define the geometry and the normals of the walls. We modified this hybrid method [44, 45] and discuss the details in the following.

To determine the normal of boundary particles, the boundary particle generation algorithm created by Marrone et al. [59] and the normal determination method by English et al. [57] were fully adopted. As shown in Fig. 1, boundary particles are color-coded in brown and spaced in d_p from each other. Reference walls are defined by scaling the forming shape of all boundary particles with a $d_p/2$ distance inward toward material particles. The normal for the reference walls are readily determined and they are used to facilitate the calculation of normals for boundary particles. For any non-corner boundary particles w, their normalized normal $\boldsymbol{n}_w$ (shown as green arrows in Fig. 1) are determined by projecting the particles on the corresponding reference wall, which is the same as the wall normal. While for corner particles, their normals direct towards the singularity points of the guiding walls [59, 57]. The projected distance between a material particle a and a boundary particle w along the

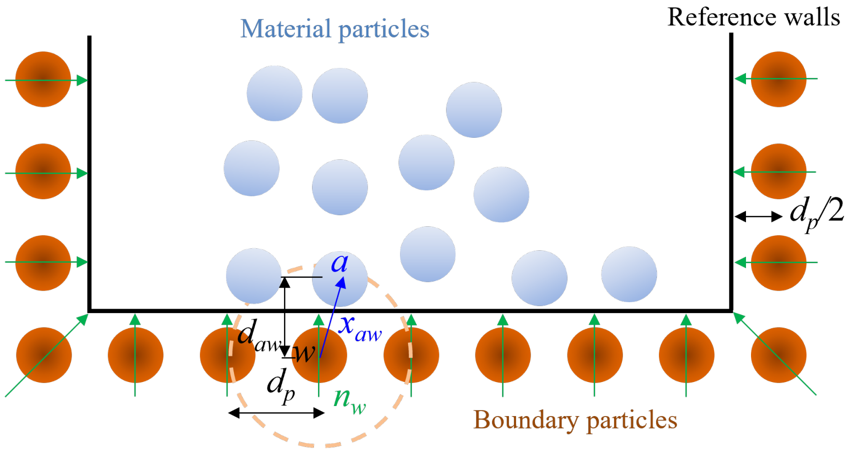

Figure 1: Illustration of the normal determination for boundary particles and the interaction between material and boundary particles.

normal direction of w is determined as:

$$d_{aw} = \boldsymbol{x}_{aw} \cdot \boldsymbol{n}_w \tag{18}$$

where $\boldsymbol{x}_{aw} = \boldsymbol{x}_a - \boldsymbol{x}_w$ is the distance vector.

For each material particle a, it only interacts with its nearest boundary particle w and only if 1) the distance between the material particle and the wall d_{aw} is shorter than the original particle spacing d_p (illustrated as the orange circle in Fig.1) and 2) the material particle is moving relatively towards the boundary:

$$d_{aw} < d_p \tag{19}$$

$$\boldsymbol{v}_{aw} \cdot \boldsymbol{n}_w < 0 \tag{20}$$

A predictor-corrector scheme is adopted to calculate the interaction force $\boldsymbol{f}_{w\to a}$ in Eq. 14 applied from boundary particle w to material particle a. At the predictor step, the boundary particles are invisible to material particles. The state variables including velocity $\boldsymbol{v}_a^\star$ and position $\boldsymbol{x}_a^\star$ are computed by considering the material-material particle interaction only. Note that the gravity term and the artificial viscosity term in Eq. 14 without taking boundary particles into account are calculated in this step. Here we use superscript * to denote "predictor" values. At the corrector step, if a material particle is close to the boundary and the criteria in Eqs. 19-20 satisfies, then, we calculate the normal component of the material-boundary interaction force as:

$$\boldsymbol{f}^{n}_{w\to a} = -\frac{\boldsymbol{n}_w[(\boldsymbol{v}^{\star}_a - \boldsymbol{v}_w)\cdot\boldsymbol{n}_w]}{\Delta t/m_a} \tag{21}$$

The above equation is obtained by using the velocity of material particle at the corrector step:

$$\boldsymbol{v}^{c}_a = \boldsymbol{v}^{\star}_a + \Delta t \cdot \frac{\boldsymbol{f}_{w\to a}}{m_a}, \tag{22}$$

and enforcing the zero relative normal velocity of the material particle with respect to the boundary:

$$(\boldsymbol{v}^{c}_a - \boldsymbol{v}_w)\cdot\boldsymbol{n}_w = 0. \tag{23}$$

Here $\boldsymbol{v}_w$ is the preassigned boundary velocity. The derivation of Eq. 21 implicitly takes two assumptions: (1) the boundary is rigid, (2) the collision between the material and the boundary is perfectly plastic (i.e., the material does not bounce back). These assumptions are valid since our targeted granular material is biomass with high compressibility and the handling equipment is made of steel, which can be treated as rigid bodies. For the non-perfect-plastic-collision and non-rigid walls, readers can find similar derivations in other literature [44, 46].

The tangential component of the interaction force $\boldsymbol{f}_{w\to a}$ depends on the slip modes, including free-slip, no-slip, and frictional slip. For the free-slip mode, the tangential force is always zero:

$$\boldsymbol{f}^{\tau}_{w\to a} = \boldsymbol{0}, \quad \text{free-slip} \tag{24}$$

For the non-slip mode, the relative velocity of the material particle towards the boundary particle must be zero in the tangential direction, namely:

$$\|(\boldsymbol{v}^{c}_a - \boldsymbol{v}_w) - [\boldsymbol{n}_w\cdot(\boldsymbol{v}^{c}_a - \boldsymbol{v}_w)]\boldsymbol{n}_w\| = 0 \tag{25}$$

We thus derive the tangential force by substituting Eq. 22 into Eq. 25 as:

$$\boldsymbol{f}^{\tau}_{w\to a} := \boldsymbol{f}^{\tau,no-slip}_{w\to a} = \frac{(\boldsymbol{v}^{\star}_a - \boldsymbol{v}_w) - [\boldsymbol{n}_w\cdot(\boldsymbol{v}^{\star}_a - \boldsymbol{v}_w)]\boldsymbol{n}_w}{\Delta t/m_a}, \quad \text{no-slip} \tag{26}$$

For the frictional slip mode with a friction coefficient μ, the tangential force is written as:

$$\boldsymbol{f}^{\tau}_{w\to a} = \begin{cases} \boldsymbol{f}^{\tau,no-slip}_{w\to a}, & \|\boldsymbol{f}^{\tau,no-slip}_{w\to a}\| < \mu\|\boldsymbol{f}^{n}_{w\to a}\| \\ \mu\|\boldsymbol{f}^{n}_{w\to a}\|\frac{\boldsymbol{f}^{\tau,no-slip}_{w\to a}}{\|\boldsymbol{f}^{\tau,no-slip}_{w\to a}\|}, & \text{otherwise} \end{cases} \tag{27}$$

With all components updated above, the correct reaction force applied from the material particles to the boundary particle is:

$$\boldsymbol{f}_{a\to w} = \sum_{a\in s} \boldsymbol{f}_{w\to a} \tag{28}$$

At the corrector step, we also assign the correct interaction forces to each boundary particle. These forces can then be summed up to obtain the reactive forces and reactive moment of the boundary with interests.

2.5. Constitutive model

A constitutive model is essential for updating the stress tensor in the momentum equation 14 at each time increment. The flow behavior of granular biomass materials is complex and needs sophisticated constitutive models. Based on the continuum model reviewed by Jin et al. [28] and the successful application for modeling granular woody biomass [23, 24], we adopt the Gudehus-Bauer (G-B) hypoplastic model [50, 51, 60] to calculate the stress rate from the velocity field.

The G-B hypoplastic model has 8 material parameters, including the granulate hardness h_s, a constant that considers the pressure-sensitivity of a grain skeleton n, critical friction angle ϕ_c, minimum, critical and maximum void ratio at zero pressure e_{d0}, e_{c0} and e_{i0}, a constant that governs the peak shear stress behavior α, and a constant that increases the incremental stiffness with increasing density and pressure β. These parameters can be calibrated from experimental characterization [60, 23]. The G-B model is expressed in rate form as:

$$\mathring{\sigma}_{ij} = f(e, \boldsymbol{\sigma}, \dot{\boldsymbol{\epsilon}}) = f_s\left[L_{ij}(\hat{\sigma}_{kl}, \dot{\epsilon}_{kl}) + f_d N_{ij}(\hat{\sigma}_{ij})\sqrt{\dot{\epsilon}_{kl}\dot{\epsilon}_{kl}}\right] \tag{29}$$

$$\dot{e} = (1+e)\dot{\epsilon}_{kk} \tag{30}$$

where $\mathring{\boldsymbol{\sigma}} = \dot{\boldsymbol{\sigma}} - \dot{\boldsymbol{\omega}} \cdot \boldsymbol{\sigma} + \boldsymbol{\sigma} \cdot \dot{\boldsymbol{\omega}}$ is the objective (Jaumann) stress-rate tensor, $\hat{\sigma}_{ij} = \sigma_{ij}/\sigma_{kk}$ is the normalized stress tensor, $\dot{\boldsymbol{\epsilon}}$ is the strain rate tensor defined in Eq. 12, and $\dot{\boldsymbol{\omega}}$ is the anti-symmetrical spin tensor and can be calculated as

$$\dot{\boldsymbol{\omega}} = 1/2\Big(\nabla \boldsymbol{v} - (\nabla \boldsymbol{v})^T\Big). \tag{31}$$

The linear and non-linear contribution terms L_{ij} and N_{ij} are resulting tensor functions, and they are expressed as

$$L_{ij} = a_1^2 \dot{\epsilon}_{ij} + \hat{\sigma}_{ij}(\hat{\sigma}_{kl}\dot{\epsilon}_{kl}), \quad N_{ij} = a_1(\hat{\sigma}_{ij} + \hat{\sigma}^*_{ij}) \tag{32}$$

with

$$\begin{aligned}
&a_1^{-1} = c_1 + c_2\sqrt{\hat{\sigma}^*_{kl}\hat{\sigma}^*_{lk}}[1 + \cos(3\theta)] \\
&c_1 = \sqrt{\frac{3}{8}}\Big(\frac{3 - \sin\phi_c}{\sin\phi_c}\Big), \quad c_2 = \frac{3}{8}\Big(\frac{3 + \sin\phi_c}{\sin\phi_c}\Big) \\
&cos(3\theta) = -\frac{\sqrt{6}\hat{\sigma}^*_{kl}\hat{\sigma}^*_{lm}\hat{\sigma}^*_{mk}}{\Big(\hat{\sigma}^*_{kl}\hat{\sigma}^*_{lk}\Big)^{1.5}}
\end{aligned}$$

where $\hat{\sigma}^*_{ij} = \hat{\sigma}_{ij} - \frac{1}{3}\delta_{ij}$ is the normalized deviatoric stress tensor, and θ is the Lode angle. Coefficients f_s and f_d in Eq. 29 are defined as:

$$\begin{aligned}
&f_s = f_b f_e \\
&f_b = \frac{h_s}{n h_i}\Big(\frac{1 + e_i}{e_i}\Big)\Big(\frac{e_{i0}}{e_{c0}}\Big)^{\beta}\Big(-\frac{\sigma_{kk}}{h_s}\Big)^{1-n} \\
&f_e = \Big(\frac{e_c}{e}\Big)^{\beta} \\
&f_d = \begin{cases} \Big(\frac{e - e_d}{e_c - e_d}\Big)^{\alpha} & e \geq e_d \\ 0 & e < e_d \end{cases} \\
&h_i = \frac{1}{c_1^2} + \frac{1}{3} - \Big(\frac{e_{i0} - e_{d0}}{e_{c0} - e_{d0}}\Big)^{\alpha}\frac{1}{c_1\sqrt{3}}
\end{aligned}$$

The coefficients f_e and f_d are pyknotropy factors, with f_e controlling the proportional expansion/contraction of the response envelope and f_d controlling the dependence of shear strength on density and pressure [50, 51]. f_b is a barotropy factor. f_s and f_d consider the influence of the void ratio and pressure level on the stress and satisfy the critical state condition. The G-B model also defines a min-max void ratio limits (e_i-e_d) along with a void ratio at critical state e_c that evolves with stress as

$$\frac{e_i}{e_{i0}} = \frac{e_d}{e_{d0}} = \frac{e_c}{e_{c0}} = \exp\Big[-\Big(\frac{-\sigma_{kk}}{h_s}\Big)^n\Big]. \tag{33}$$

Note void ratio is allowed to exceed the limits. When $e < e_d$, the sample becomes a dry masonry that could sustain vertical loads without any horizontal support, and the pyknotropy factor $f_d = 0$, which indicates the model collapses into a hypoelastical mode [51, 60]. When $e > e_i$, the sample either has macro-voids in the grain skeleton or has open grain contacts [60]. However, we pull back e once it exceeds e_i ($e = e_i$, if $e > e_i$) in the SPH code implementation, which avoids the unrealistic low bulk density and high skeleton volume. This numerical adjustment does not destroy the conservation of mass because each SPH particle bears a constant mass once created. Thus, bulk density and volume represented by an SPH particle change simultaneously to keep a constant mass. In addition, this numerical correction ensures an accurate and robust updating of particle state for neighboring particles. Noted that the parameters h_s and n are calibrated from an axial compression test (similar to the setting in Section 3.4) to satisfy

$$\frac{e}{e_0} = \exp\Big[-\Big(\frac{-\sigma_{kk}}{h_s}\Big)^n\Big]. \tag{34}$$

Thus, e will not exceed the $[e_d, e_i]$ limit under a similar stress evolution. Numerical simulation of all presented cases in this paper also demonstrated the evolution of void ratio is within limits. To summarize, the mass conservation equation reformulated by replacing density with void ratio greatly simplifies the implementation and it fits naturally with the void ratio evolution (Eq. 30), as we stated in Section 2.2.

2.6. Explicit time integration

A symplectic position Verlet time integration scheme has second-order accuracy in time and is thus implemented to ensure the robustness of the SPH solver. In this scheme, the state variables need to be updated in the middle of a time step, i.e. $t + \Delta t/2$. Recall the boundary treatment needs a predictor-corrector scheme for each increment, thus, we first obtain the predictor values of velocity $\boldsymbol{v}^{\star}$ and position $\boldsymbol{x}^{\star}$ and update the correct stress $\boldsymbol{\sigma}$ and void ratio e values at the predictor step for the time increment from t to $t + \Delta t/2$ as:

$$\boldsymbol{v}_a^{t+\Delta t/2,\star} = \boldsymbol{v}_a^t + \frac{\Delta t}{2}\boldsymbol{a}_a^t \tag{35}$$

$$\boldsymbol{x}_a^{t+\Delta t/2,\star} = \boldsymbol{x}_a^t + \frac{\Delta t}{2}\boldsymbol{v}_a^t \tag{36}$$

$$\boldsymbol{\sigma}_a^{t+\Delta t/2} = \boldsymbol{\sigma}_a^t + \frac{\Delta t}{2}(\dot{\boldsymbol{\sigma}}_a)^t \tag{37}$$

$$e_a^{t+\Delta t/2} = e_a^t + \frac{\Delta t}{2}(\dot{e}_a)^t \tag{38}$$

where $\boldsymbol{a}_a^t$ stands for the acceleration of particle a at time t, it is calculated by summing up all the three terms on the right side of Eq. 14 except the boundary-material interaction term $\boldsymbol{f}_{w\to a}/m_a$. This term is taken into account at the corrector step to obtain the correct velocity and position following the scheme detailed in Section 2.4:

$$\boldsymbol{v}_a^{t+\Delta t/2} = \boldsymbol{v}_a^{t+\Delta t/2,\star} + \frac{\Delta t}{2}\frac{\boldsymbol{f}_{w\to a}^{t+\Delta t/2}}{m_a} \tag{39}$$

$$\boldsymbol{x}_a^{t+\Delta t/2} = \boldsymbol{x}_a^{t+\Delta t/2,\star} \tag{40}$$

These correct values at time $t + \Delta t/2$ are then used to calculate the state variable at time $t + \Delta t$ via:

$$\boldsymbol{v}_a^{t+\Delta t,\star} = \boldsymbol{v}_a^{t+\Delta t/2} + \frac{\Delta t}{2}\boldsymbol{a}_a^{t+\Delta t/2} \tag{41}$$

$$\boldsymbol{x}_a^{t+\Delta t,\star} = \boldsymbol{x}_a^{t+\Delta t/2} + \frac{\Delta t}{2}\boldsymbol{v}_a^{t+\Delta t/2} \tag{42}$$

$$\boldsymbol{\sigma}_a^{t+\Delta t} = \boldsymbol{\sigma}_a^{t+\Delta t/2} + \frac{\Delta t}{2}(\dot{\boldsymbol{\sigma}}_a)^{t+\Delta t/2} \tag{43}$$

$$e_a^{t+\Delta t} = e_a^{t+\Delta t/2} + \frac{\Delta t}{2}(\dot{e}_a)^{t+\Delta t/2} \tag{44}$$

Similar to the updating algorithm at the start of the time increment, the velocity and position values do not account for the boundary interaction and need to be corrected through the following equation:

$$\boldsymbol{v}_a^{t+\Delta t} = \boldsymbol{v}_a^{t+\Delta t,\star} + \frac{\Delta t}{2}\frac{\boldsymbol{f}_{w\to a}^{t+\Delta t}}{m_a} \tag{45}$$

$$\boldsymbol{x}_a^{t+\Delta t} = \boldsymbol{x}_a^t + \frac{\Delta t}{2}(\boldsymbol{v}_a^t + \boldsymbol{v}_a^{(t+\Delta t)}) \tag{46}$$

We also adopted a variable time step Δt as:

$$\Delta t = C_{CFL} \frac{h}{\max(c_s, 10 \cdot \max\|\boldsymbol{v}_a\|) + \max_a(\mu_{ab})} \tag{47}$$

in which a Courant-Friedrich-Levy condition $C_{CFL} = 0.2$ is used [61, 49]. The artificial viscosity μ_{ab} is calculated as:

$$\mu_{ab} = \max_b \frac{h\boldsymbol{v}_{ab} \cdot \boldsymbol{x}_{ab}}{x_{ab}^2 + 0.01h^2}. \tag{48}$$

The framework of SPH was proposed in 1970s, and it has not been widely adopted in literature until recently due to its high computational cost. The rapid development of GPU hardware as well as the explicit Lagrangian algorithm of SPH make it possible, and cost effective, for a wide variety of scientific computations, including granular material flow modeling. The GPU implementation algorithm in DualSPHysics [49] was adopted with an updated neighbor particle list and force computation and state variable updating using CUDA codes. The data transfer between CPU and GPU memories is only activated at the start of simulation and at the time increment of data output to accelerate the computation. The axial compression test of pine chips, for example, has a domain discretized into 56175 particles and with 15 seconds of physical time for conducting the test, the GPU code only runs for 1.7 hours. The same example took 75.8 hours using the CPU code. Note the current implementation only works for a single NVIDIA GPU, multi-GPU implementation is under development.

3. Numerical Examples

Four examples were simulated to validate the theory and demonstrate the capability of the SPH solver. The numerical stability of the simulations and validation of the boundary treatment are discussed in detail.

3.1. Inclined Sliding - Elastic Block

An elastic cubic block sliding along slopes with different inclinations and coefficients of friction was modelled to verify the implemented boundary treatments. The elastic block with a dimension of $0.32\,m \times 0.32\,m \times 0.32\,m$ was discretized by $25 \times 25 \times 25$ SPH material particles. We assigned the block with density $\rho = 1500\,kg/m^3$, Young's modulus $E = 8.3\,MPa$ and Poisson's ratio $\nu = 0.2$. The speed of sound c_s required for artificial viscosity term in Eq. 16 can be determined via $c_s = \sqrt{(M/\rho)}$, where M is the Constraint Modulus given by $M = \frac{E(1-\nu)}{(1+\nu)(1-2\nu)}$. For the rest of the simulation parameters, we used the initial inter-particle distance for both the elastic block and the sliding plane as $d_p = 0.013\,m$, a kernel size of $h = \sqrt{3}d_p$, and a coefficient of artificial viscosity $\alpha_\mu = 0.1$.

Fig. 2(a) shows the positions of an elastic block on an inclination $\theta = 20°$ plane with different wall treatments of no-slip, frictional slip, and free-slip at time $t = 0s$, $1s$, and $2s$. The no-slip condition successfully guarantees the block does not slide while the block with a frictional slip boundary travels slower than the case with a free-slip boundary, as expected. To quantitatively validate the frictional boundary implementation, a series of cases with different inclination angles and frictional coefficients were simulated. The traveling displacement against time obtained from these simulations was compared with the analytical solution as shown in Fig. 2(b). Excellent agreement was found between numerical and analytical results for inclination $\theta = 20°$ and $40°$, and for both free-slip and frictional slip cases. Fig. 2(b) also shows the solver is capable of realizing no movement for the critical cases at a critical frictional angle (i.e., $\theta = \arctan(\mu) = 20°/40°$, color-coded in yellow).

3.2. Column Collapse - Sand

The collapse of a sand column was simulated and the results were compared with values reported in the literature [62] to verify the implementation of G-B constitutive model. As illustrated in Fig.3(a), the sand column collapse experiments were carried out by lifting a cylindrical column packed with dry sand at a velocity of roughly 2.0 m/s. Lube et al.[62] reported the shape evolution of resulting sand dune for the cases with different initial height to radius aspect ratio h_i/r_i. We constructed the same experimental setup and followed the same procedure for the SPH numerical simulation. The G-B constitutive model described in Section 2.5 with Karlsruhe sand parameters was used since the mechanical behavior of Karlsruhe sand is very close to the sand used for those experiments and the critical parameter

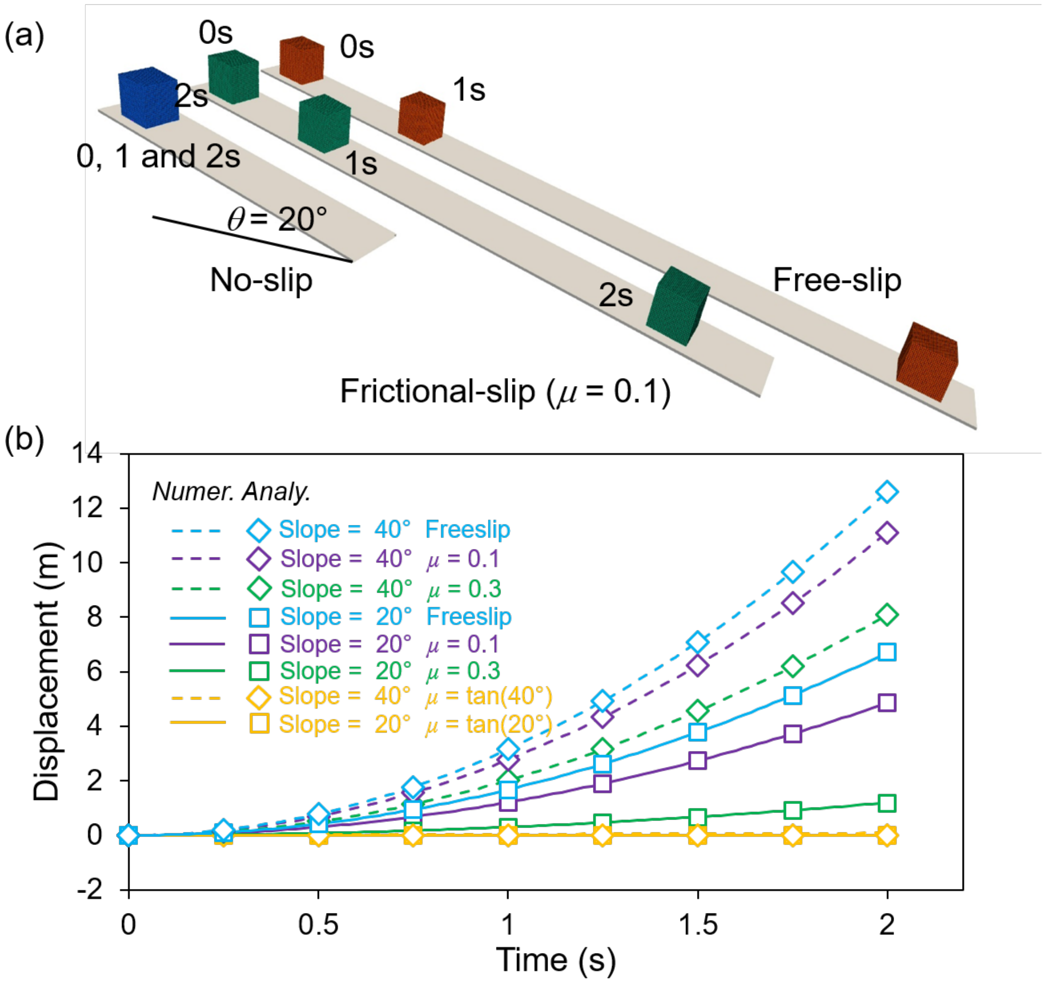

Figure 2: Simulation of an elastic block slides on a slope: (a) Snapshots of block positions at $t = 0$, 1 and $2\,s$ on a 20° slope with no-slip, frictional-slip ($\mu = 0.1$) and free-slip boundary conditions; (b) Comparison of simulation predicted displacement against time with analytic solutions for different cases with different slopes and frictional coefficients (continuous and dashed curves denote numerical results, squares and diamonds represent analytical solutions).

Table 1: G-B hypoplastic model parameters for Karlsruhe sand, adopted from Herle et al. [60].

$\phi_c[^\circ]$	$h_s[MPa]$	$n[-]$	$e_{d0}[-]$	$e_{c0}[-]$	$e_{i0}[-]$	$\alpha[-]$	$\beta[-]$
30	5800	0.28	0.53	0.84	1.0	0.13	1

that influences the column collapse is internal friction angle. The Karlsruhe sand parameters calibrated by Herle et al. [60] are listed in Table 1.

For all simulations, the sand solid density ρ_s was set to $2650\,kg/m^3$, and the initial void ratio e_0 was chosen as 0.9 to represent a relatively loosely packed sample, which gave an initial bulk density of $\rho = 1395\,kg/m^3$. We used a wall friction coefficient $\mu = 0.577$, corresponding to a friction angle of 30°, a kernel size of $h = \sqrt{3}d_p$ as the rule of thumb, and an artificial viscosity coefficient of $\alpha_\mu = 0.1$. The G-B hypoplastic model does not include a parameter that can be directly linked to the speed of sound, but trial-and-error showed a $c_s = 120\,m/s$ gives reasonable results. A total of eight simulation cases were conducted with a fixed initial sample radius $r_i = 0.08\,m$ and variable column heights, which resulted in cases with aspect ratios at h_i/r_i =0.5, 1.0, 1.7, 2.0, 3.0, 4.0, 6.0 and 7.0.

Fig. 3(b) shows the predicted density distribution at the final deposition of the sand dune. The center part of the sand column remains intact when the initial aspect ratio is low, while a greater volume of sand particles in the center of the column are disturbed as the aspect ratio increases. The case of $h_i/r_i = 0.5$ even shows a flat top at the final stage. These predictions match experimental observation [62]. In Fig. 3(c-d), we quantitatively compare the change of two dimensionless numbers with different initial aspect ratios. The first dimensionless number is defined as $(r_\infty - r_i)/r_i$ with r_∞ denoting the final radius of sand dune. The experiment results indicate that the slope of the dimensionless number against the aspect ratio has constant but different values in logarithmic scale for the data set below and above $h_i/r_i = 0.7$. Fig. 3(c) clearly shows the numerical prediction (marked as circles) successfully repeats this phenomenon. The second dimensionless number is defined as $\sqrt{(r_\infty - r_i)^2 + h_i^2}/V_i^{1/3}$ with V_i representing the initial sample volume. As shown in Fig.3(d), a linear relationship is obtained for both the experimental and numerical results, again demonstrating the correctness of implemented G-B hypoplastic model.

3.3. Angle of Repose - Granular Biomass

After the frictional boundary condition and the G-B hypoplastic model implementation were successfully validated, the solver for modeling granular biomass was tested. The flow behavior of milled loblolly pine chips was investigated by modeling the Angle of Repose (AoR) test, a simple and common test used extensively to study the flowability of granular materials [63, 17]. The milled pine chips were obtained by a series of processing procedures including chipping, grinding, and drying to have a particle size distribution of $D_{50} = 1\,mm$. Details about the sample preparation can be found in [64, 23]. The AoR experiments were conducted similarly to the column collapse test in Section 3.2 with minor changes: an acrylic cylinder was filled with pine chips to a designated height using the dry pluviation method, which can obtain an initially loosely packed sample. The mass was recorded, along with the height, to calculate the initial void ratio e_0. The prepared column was then released by lifting the acrylic cylinder at a quasi-static velocity of 5 cm/s to spread the pine chips out onto an acrylic base. We performed four sets of tests with different initial height-to-diameter ratios at H/D = 15.24/5.08, 20.32/5.08, 30.48/10.16, and 40.64/10.16 cm. For each H/D set, ten trails were repeated to ensure the robustness of the experimental results. Fig. 4(a) shows representative pictures that were used to determine AoRs for all trials. A thin layer of pine particles spread out far on the base in all cases, which results in an unrealistically low AoR value if considered. Thus, the height of the pine dune was divided evenly into 4 layered sections and the AoR was determined from the second layer. For each picture, two AoRs were measured for both the left- and right-hand sides. The coefficient of friction between the pine chips and the acrylic surface was also determined by allowing a block of pine chips to slide along a plane with variable inclinations (see supplementary information Section S1 for details). The measured value is $\mu = 0.397 \pm 0.024$.

Four simulations with the exact same initial geometry and void ratio as the experiments were performed to model the pine chip AoR test. The physical and numerical parameters, including a speed of sound $c_s = 120\,m/s$, a kernel size of $h = \sqrt{3}d_p$, a coefficient of wall

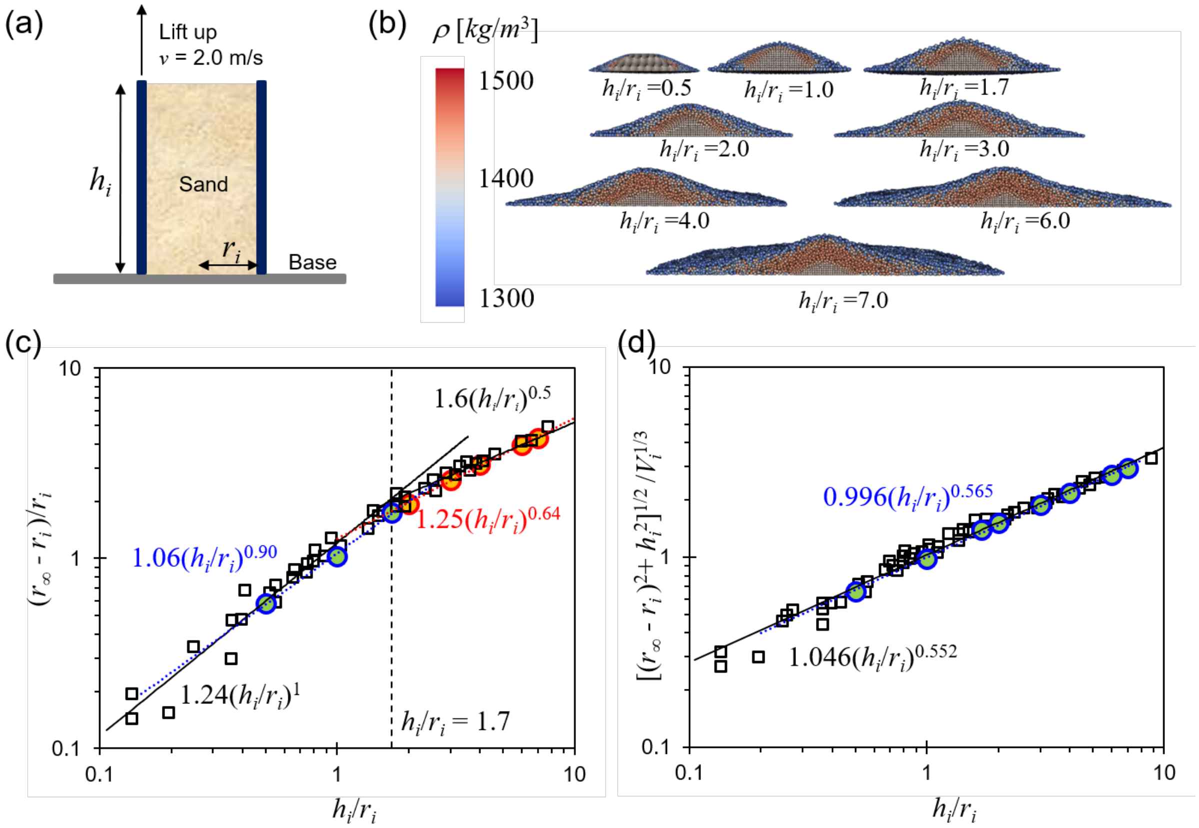

Figure 3: Sand column collapse tests: (a) Schematic sketch of the experimental setup; (b) The predicted distribution of bulk density on the final sand deposit for different initial aspect ratios h_i/r_i; (c) and (d) Comparison of dimensionless numbers against aspect ratio between experimental measurements and numerical predictions, in which r_∞ is the final radius of the dune and V_i is the initial volume of the sand column. Black squares denote experimental data from [62], and circles mark numerical results. Two colors are used in (c) to distinguish the 2 data regimes.

Table 2: G-B hypoplastic model parameters for pine chips, adopted from Lu et al. [23].

$\phi_c[^\circ]$	$h_s[kPa]$	$n[-]$	$e_{d0}[-]$	$e_{c0}[-]$	$e_{i0}[-]$	$\alpha[-]$	$\beta[-]$
47.3	187.6	0.30	0.50	1.06	1.38	0.3	1.0

friction at $\mu = 0.397$ (corresponding to a friction angle of 21.6°), and a coefficient of artificial viscosity at $\alpha_\mu = 0.3$, were kept the same and used for all simulations. The particle solid density $\rho_s = 430\,kg/m^3$ was based on previous studies [65, 66, 25, 23]. For this particular biomass sample, the calibrated G-B hypoplastic model parameters were reported by Lu et al. [23] and adopted in this study (see Table 2).

Fig. 4(b) shows a predicted bulk density map from an AoR simulation at the end of settlement. The numerical AoR values were determined by first obtaining the height of the dune by locating the highest SPH particle as h_{max}. The final shape of pine chips was then sliced into 4 evenly-distributed sections in height shown in Fig. 4(c). The radius of disks that overlap with the particles in the second and third planes were determined by averaging the distance between the center and the furthest particles along the 16 directions, which are depicted as red lines in Fig. 4(d) and evenly-spaced across the entire disk. The numerical AoR was then determined by using the radius and heights of the two disks, similar to the experimental measurement procedure.

The quantitative comparison between the experimental and numerical AoR results is summarized in Table 3. The numerical results under the column of "base cases" are obtained by using the simulation parameters given in the previous paragraph, they all share good agreement with the experimental data as all four results fall within one standard deviation range deviating from the mean values of the experimental values. To examine how the SPH parameters affect the numerical AoR, further simulations were conducted with the speeds of sound $c_s = 80, 120\,m/s$, coefficients of artificial viscosity $\alpha_\mu = 0.1, 0.5$, kernel sizes $h = 0.8\sqrt{3}d_p$, $1.2\sqrt{3}d_p$ and cylinder lifting velocities $v = 2.5, 7.5\,cm/s$ for each of the four different H/D cases. The minimum and maximum AoRs obtained from these simulations are also listed in Table 3. To summarize, the speed of sound has a marginal effect on the

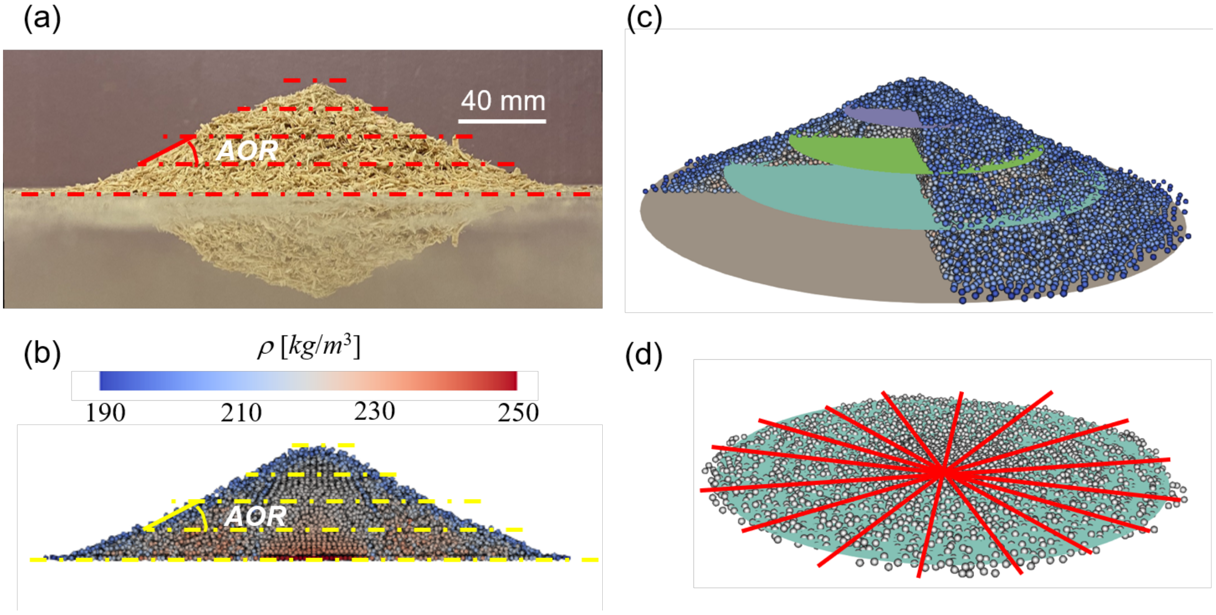

Figure 4: Comparison of Angle of Repose (AoR) for pine chips between physical experiment and numerical simulation: (a) Experimental measurement of AoR of a case with initial H/D = 15.24/5.08 cm; (b) Predicted pine pile with the same H/D ratio ; (c) Demonstration of 4 equal-height segments over the pine pile; (d) Sketch to determine the radius of each layer by averaging the length over 16 directions.

Table 3: Comparison between experimental and numerical AoR results for pine chips.

H/D (cm)	Initial void ratio, e_0	Experimental AoR		Numerical AoR		
		Mean	Standard deviation	Base case	Min.	Max.
15.24/5.08	1.107	24.4°	3.38°	26.25°	22.37°	29.27°
20.32/5.08	0.975	25.5°	1.60°	24.31°	22.54°	28.38°
30.48/10.16	0.876	23.6°	2.14°	25.80°	23.81°	30.24°
40.64/10.16	0.878	24.6°	2.27°	25.84°	24.27°	28.94°

results with slightly decreasing AoR for a higher c_s. This is exclusively caused by an increase of artificial viscosity term as c_s is linearly proportional to artificial viscosity (Eq. 16). The step size change due to a change in c_s (Eq. 47) does not affect the results if a constant artificial viscosity is used. An increase in the artificial viscosity coefficient also reduces AoR with a more spread dune and a sharper top. Kernel size has the most notable impact on AoR as a larger kernel size increases AoR. A higher uplifting velocity causes a wider spread sample with a flatter top and a lower AoR. The proper choice of these parameters, especially the artificial viscosity and kernel size, is important to ensure the accuracy of SPH simulations. Detailed investigation of the effect of SPH parameters on AoR can be found in supplementary material Section S2.

3.4. Axial Compression - Granular Biomass

The second simulation example for milled loblolly pine is the constraint 1-D axial compression test, which was used to validate the capability of SPH code for modeling the high compressibility of granular biomass. The physical experiments were conducted by first filling a cell with a diameter of 119 mm with pine chips up to a designated height and an initial void ratio. Then the top lid was loaded to compress the sample with a rate of 0.083 mm/s until a certain loading stress was reached followed by unloading at the same rate. The traveling displacement and the reaction force of the lid were monitored and recorded during the whole loading process. Several trials were performed for each case to reduce human-induced error.

The SPH simulations followed the same procedure as the experiment with only the loading rate changed to 1 mm/s to reduce the computation cost. Note this change is valid since the G-B hypoplastic model is a quasi-static constitutive law, which does not depend on the loading rate theoretically. The results with different loading rates were also carefully examined, and no dynamic effects were observed. We used a speed of sound $c_s = 80m/s$, a kernel size $h = 0.6\sqrt{3}d_p$, a coefficient of artificial viscosity $\alpha_\mu = 0.3$, and a wall friction coefficient $\mu = 0.397$ for all three loading cases with maximum loading stresses at 1kPa, 5kPa, and 10 kPa. The initial sample heights and void ratios are 83, 86, 86 mm and 0.72, 0.78, 0.78, respectively, in accordance with the average initial values from the experimental measurements. Note the smaller kernel size was used for stability at high pressure and will be discussed in detail later.

Fig. 5 shows a series of snapshots of predicted vertical stress, void ratio, and wall reaction stress at different loading/unloading stages. Vertical stress is generally uniformly distributed during loading but relaxed more for the upper part when unloading. This is physically expected since the stress of the lower part cannot be efficiently released due to particle interlocking and wall friction. Some stress instability near the top and bottom boundaries was observed, which is because the artificial viscosity term (Eq. 14) for the material particles near the boundary does not have a full kernel support. As a result, nonphysical energy is not fully dissipated. The adopted contact model can also contribute to stress instability given a denser particle number near the boundary is predicted. Note increasing the number of particles in a kernel can further increase the chance of numerical instability. Even though the stress in the material near the lid is not uniformly distributed, the reactive stress of all walls is uniform during loading and unloading except minimum in-homogeneity is observed for the top lid under the unloading condition. Fig. 5 also shows a dramatic decrease during loading for the void ratio, but negligible rebounding is predicted as expected.

As shown in Fig. 6, experimental and numerical results are plotted together in terms of stress-strain (Fig. 6(a)) and void ratio-stress (Fig. 6(b)) relationships. In which $P_s = (\sigma_x + \sigma_y + \sigma_z)/3 = \frac{(1+2k_0)}{3}\sigma_z$ with k_0 denoting the lateral earth pressure coefficient at rest. $k_0 = 1/3$ is assumed for both the experiments and simulations. The numerical results are

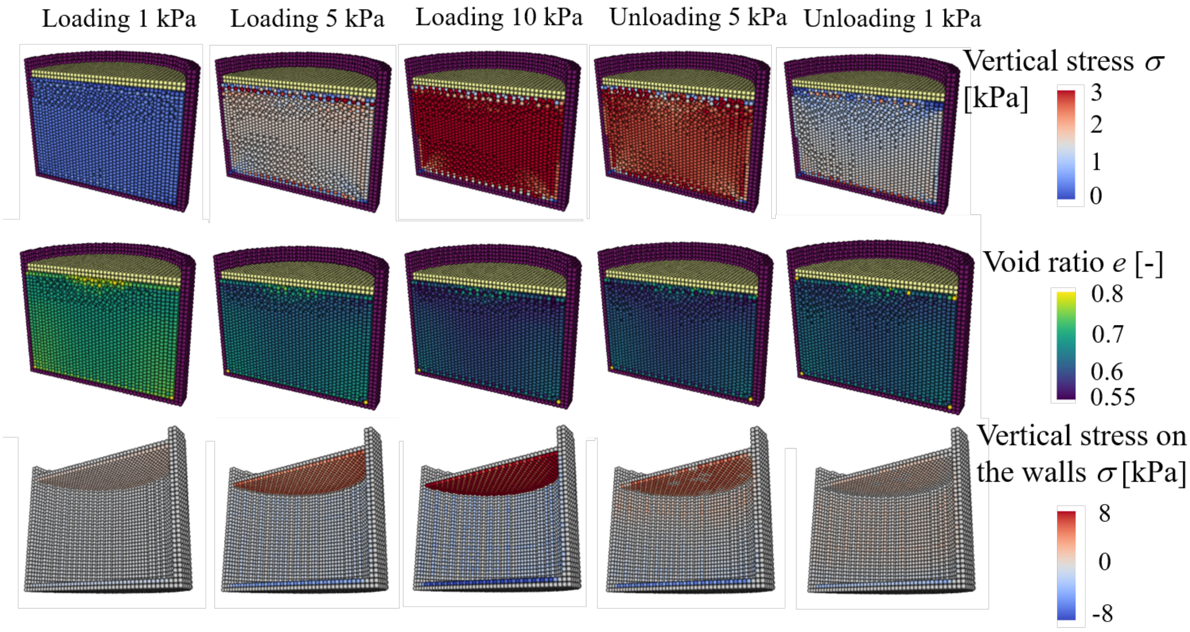

Figure 5: Simulation results of evolving vertical stress (first row), void ratio (second row), and wall vertical stress (third row) from an axial compression test of milled loblolly pine loaded up to 10 kPa followed by unloading

plotted in solid curves, while the experimental results are shown in error bar format. For a given loading stress, the error bar is centered on the mean experimental value and spans with a length of standard derivation in both directions of vertical strain (Fig.6(a)) and void ratio (Fig. 6(b)), respectively. The SPH simulation successfully reproduces the axial compression test for both the loading and unloading stress paths. A slight mismatch is observed for the case with a maximum of 10 kPa compression during the unloading stage. This is because the adopted G-B hypoplastic model cannot fully capture the mechanical behavior of pine chips, in particular, the model underestimates the inelastic rebounding when unloaded.

3.5. Discussion

Numerical stability. SPH is prone to generate stress oscillation, which is known as short-length-scale noise [67, 37] and observed in the axial compression simulation example in Section 3.4. During the loading stage under compression, more particles are squeezed into the kernel with a fixed kernel size, making the stress oscillation more severe. This oscillation

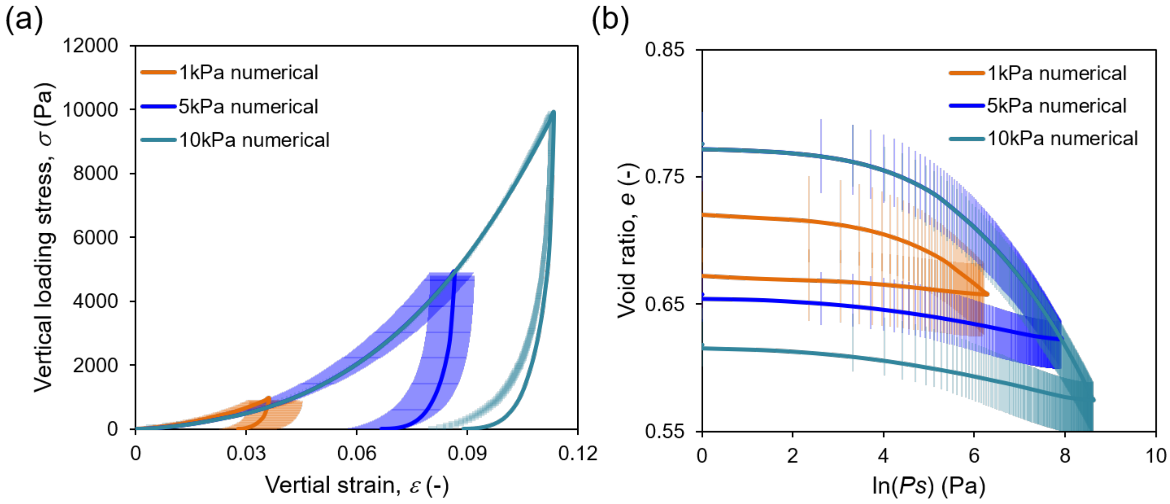

Figure 6: Comparison of axial strain-stress responses (a) and void ratio-mean stress relationships (b) between the experimental measurements and numerical predictions of axial compression tests for pine chips.

is especially prominent when the material particles are near the boundary. This noise can be mitigated by reducing the kernel size. However, care should be taken as a too-small kernel size will dramatically compromise the accuracy. Instead of using a small kernel, adaptively adjusting the smoothing kernel depending on particle concentration is a more promising mitigation for the noise [68, 56]. Alternatively, instability mitigation can be achieved by maintaining relatively even-distributed particles within a kernel [69]. A number of treatment techniques, such as the particle number-density constraint[70], particle shifting [34, 71, 72], and transport formulation [73, 74] has been proposed to maintain particle uniform distribution. The third approach to alleviate stress oscillation is to regularize the stress distribution. At the end of each designated time step, the stress of all particles is recalculated by smoothing the stress field over neighboring particles using moving least square [37] or kernel-weighted averaging [39] regularization methods. The fourth approach proposed in the literature is to replace the artificial viscosity term with a more robust energy dissipation strategy, including the viscous damping [37] and stress diffusion [42] methods. Among all these mitigation approaches, we tested the kernel-weight averaging and stress diffusion methods for our axial compression simulation. Both methods failed to provide robust results, while a small kernel of $h = 0.6\sqrt{3}d_p$ yielded satisfactory results. In addition to the short-length-scale noise, SPH also suffers from shock waves when there is a sudden change in loading conditions. This is commonly observed when gravity is suddenly applied at the first time step. We added the gravity gradually within a time range to effectively mitigate the initial shock wave for all our simulations. This treatment also improves the gravity-induced uneven particle distribution and slightly improves the simulation quality.

Boundary treatment. Before adopting the hybrid boundary treatment described in Section 2.4, the dummy boundary particle method was first implemented with stress tensors of boundary particles either updated by extrapolating the stress value of the neighboring material particles [47] or assigned with the same values as the largest stress tensor of the neighboring material particles [41]. Both techniques result in material particles penetrating through boundary particles for the AoR and axial compression tests, and the penetrating magnitude and the number of penetrating particles significantly increase if the relative movement between material and boundary particles gets faster. These results demonstrate the particle-particle dummy boundary method cannot provide sufficient repulsive force, while the later adopted hybrid method successfully addresses the penetrating issue for all cases. One challenge associated with the hybrid method is determining the normal for corner boundary particles. First, the method proposed by Zhan et al. [45] was adopted, in which the normal is determined by connecting the corner particle to a specific material particle with the closest distance. Thus, the normal changes in each time step according to different boundary-material particle pairs and the material particle location. Stress instability nucleated from the corner material particles from the axial compression simulations was observed. After changing to the method proposed by Marrone et al. [59], the constant normal assignment for corner particles was more robust and accurate for all the simulation cases tested in this study.

4. Conclusion

This study introduces a novel SPH framework for modeling granular biomass flow. This framework includes modifications to the mass conservation governing equation, boundary conditions with the choice of frictional, no-slip and free-slip contact, and a hypoplastic constitutive model, in addition to general SPH theory. These modifications were implemented using a symplectic position Verlet time integration combined with a predictor-corrector scheme in CUDA coding for GPU-parallelization. To validate the code, four numerical examples were conducted and compared to analytical solutions or experimental data. The inclined sliding and column collapse examples confirmed the effectiveness of our boundary treatment and the constitutive models. While the examples of AoR and axial compression examples demonstrated the SPH code's ability to model the flow of unconventional granular biomass. In addition, practical guidance for modeling granular biomass materials using SPH was provided. This study expands the capabilities of SPH to simulate unconventional granular materials and provides insight into the mechanics of biomass flowability, which can inform the design of handling equipment. Future studies will investigate more complex flow conditions and be reported in forthcoming papers.

Acknowledgement

This work was performed as part of the Feedstock Conversion Interface Consortium (FCIC) with funding graciously provided by the U.S. Department of Energy Bioenergy Technologies Office. This article was authored by Idaho National Laboratory, managed by Battelle Energy Alliance, under Contract No. DE-AC07-05ID14517. The views expressed in the article do not necessarily represent the views of the DOE or the U.S. Government. The U.S. Government retains and the publisher, by accepting the article for publication, acknowledges that the U.S. Government retains a nonexclusive, paid-up, irrevocable, worldwide license to publish or reproduce the published form of this work, or allow others to do so, for the U.S. Government purposes. The first and corresponding authors would like to acknowledge Dr. Cong Peng at the ESS Engineering Software Steyr GmbH for the discussion

on the SPH theory for granular flow modeling.

References

[1] WEC, Comparison of energy systems using life cycle assessment—special report (2004 July).

[2] M. Akorede, H. Hizam, M. Ab Kadir, I. Aris, S. Buba, Mitigating the anthropogenic global warming in the electric power industry, Renewable and sustainable energy reviews 16 (5) (2012) 2747–2761.

[3] L. Gustavsson, P. Börjesson, B. Johansson, P. Svenningsson, Reducing co2 emissions by substituting biomass for fossil fuels, Energy 20 (11) (1995) 1097–1113.

[4] D. Carpenter, T. L. Westover, S. Czernik, W. Jablonski, Biomass feedstocks for renewable fuel production: a review of the impacts of feedstock and pretreatment on the yield and product distribution of fast pyrolysis bio-oils and vapors, Green Chemistry 16 (2) (2014) 384–406.

[5] J. R. Hess, C. T. Wright, K. L. Kenney, Cellulosic biomass feedstocks and logistics for ethanol production, Biofuels, Bioproducts and Biorefining: Innovation for a sustainable economy 1 (3) (2007) 181–190.

[6] S. H. Shuit, K. T. Tan, K. T. Lee, A. Kamaruddin, Oil palm biomass as a sustainable energy source: A malaysian case study, Energy 34 (9) (2009) 1225–1235.

[7] F. Bilgili, E. Koçak, Ü. Bulut, S. Kuşkaya, Can biomass energy be an efficient policy tool for sustainable development?, Renewable and Sustainable Energy Reviews 71 (2017) 830–845.

[8] M. Langholtz, B. Stokes, L. Eaton, 2016 billion-ton report: Advancing domestic resources for a thriving bioeconomy, volume 1: Economic availability of feedstock, Oak Ridge National Laboratory, Oak Ridge, Tennessee, managed by UT-Battelle, LLC for the US Department of Energy 2016 (2016) 1–411.

[9] EIA, Annual energy outlook 2022 (2022).

[10] Á. Ramírez-Gómez, Research needs on biomass characterization to prevent handling problems and hazards in industry, Particulate Science and Technology 34 (4) (2016) 432–441.

[11] Z. Miao, T. E. Grift, A. C. Hansen, K. Ting, Flow performance of ground biomass in a commercial auger, Powder technology 267 (2014) 354–361.

[12] D. Ilic, K. Williams, R. Farnish, E. Webb, G. Liu, On the challenges facing the handling of solid biomass feedstocks, Biofuels, Bioproducts and Biorefining 12 (2) (2018) 187–202.

[13] N. Chevanan, A. R. Womac, V. S. Bitra, D. C. Yoder, S. Sokhansanj, Flowability parameters for chopped switchgrass, wheat straw and corn stover, Powder Technology 193 (1) (2009) 79–86.

[14] C. A. Ogden, Flow mechanics of switchgrass bulk solid in hoppers under gravity discharge, Ph.D. thesis, Purdue University (2010).

[15] M. Gil, D. Schott, I. Arauzo, E. Teruel, Handling behavior of two milled biomass: Srf poplar and corn stover, Fuel Processing Technology 112 (2013) 76–85.

[16] F. Miccio, D. Barletta, M. Poletto, Flow properties and arching behavior of biomass particulate solids, Powder technology 235 (2013) 312–321.

[17] J. Falk, R. J. Berry, M. Broström, S. H. Larsson, Mass flow and variability in screw feeding of biomass powders—relations to particle and bulk properties, Powder technology 276 (2015) 80–88.

[18] G. Qiu, S. Henke, J. Grabe, Application of a coupled eulerian–lagrangian approach on geomechanical problems involving large deformations, Computers and Geotechnics 38 (1) (2011) 30–39.

[19] S. Bandara, K. Soga, Coupling of soil deformation and pore fluid flow using material point method, Computers and geotechnics 63 (2015) 199–214.

[20] J. M. Carbonell, L. Monforte, M. O. Ciantia, M. Arroyo, A. Gens, Geotechnical particle finite element method for modeling of soil-structure interaction under large deformation conditions, Journal of Rock Mechanics and Geotechnical Engineering 14 (3) (2022) 967–983.

[21] Y. Wang, Y. Lu, J. Y. Ooi, Finite element modelling of wall pressures in a cylindrical silo with conical hopper using an arbitrary lagrangian–eulerian formulation, Powder technology 257 (2014) 181–190.

[22] J. Sarrate, A. Huerta, J. Donea, Arbitrary lagrangian–eulerian formulation for fluid–rigid body interaction, Computer Methods in Applied Mechanics and Engineering 190 (24-25) (2001) 3171–3188.

[23] Y. Lu, W. Jin, J. Klinger, T. L. Westover, S. Dai, Flow characterization of compressible biomass particles using multiscale experiments and a hypoplastic model, Powder Technology 383 (2021) 396–409.

[24] Y. Lu, W. Jin, N. Saha, J. L. Klinger, Y. Xia, S. Dai, Wedge-shaped hopper design for milled woody biomass flow, ACS Sustainable Chemistry & Engineering (2022).

[25] Y. Xia, Z. Lai, T. Westover, J. Klinger, H. Huang, Q. Chen, Discrete element modeling of deformable pinewood chips in cyclic loading test, Powder technology 345 (2019) 1–14.

[26] Y. Xia, J. J. Stickel, W. Jin, J. Klinger, A review of computational models for the flow of milled biomass part i: Discrete-particle models, ACS Sustainable Chemistry & Engineering 8 (16) (2020) 6142–6156.

[27] T. Tian, J. Su, J. Zhan, S. Geng, G. Xu, X. Liu, Discrete and continuum modeling of granular flow in silo discharge, Particuology 36 (2018) 127–138.

[28] W. Jin, J. J. Stickel, Y. Xia, J. Klinger, A review of computational models for the flow of milled biomass part ii: Continuum-mechanics models, ACS Sustainable Chemistry & Engineering 8 (16) (2020) 6157–6172.

[29] W. Jin, Y. Lu, F. Chen, A. Hamed, N. Saha, J. Klinger, S. Dai, Q. Chen, Y. Xia, On the fidelity of computational models for the flow of milled loblolly pine: A benchmark study on continuum-mechanics models and discrete-particle models, Frontiers in Energy Research 10 (2022).

[30] R. A. Gingold, J. J. Monaghan, Smoothed particle hydrodynamics: theory and application to non-spherical stars, Monthly notices of the royal astronomical society 181 (3) (1977) 375–389.

[31] L. B. Lucy, A numerical approach to the testing of the fission hypothesis, The astronomical journal 82 (1977) 1013–1024.

[32] X. Y. Hu, N. A. Adams, A multi-phase sph method for macroscopic and mesoscopic flows, Journal of Computational Physics 213 (2) (2006) 844–861.

[33] M. Antuono, A. Colagrossi, S. Marrone, D. Molteni, Free-surface flows solved by means of sph schemes with numerical diffusive terms, Computer Physics Communications 181 (3) (2010) 532–549.

[34] S. J. Lind, R. Xu, P. K. Stansby, B. D. Rogers, Incompressible smoothed particle hydrodynamics for free-surface flows: A generalised diffusion-based algorithm for stability and validations for impulsive flows and propagating waves, Journal of Computational Physics 231 (4) (2012) 1499–1523.

[35] H. H. Bui, K. Sako, R. Fukagawa, Numerical simulation of soil–water interaction using smoothed particle hydrodynamics (sph) method, Journal of Terramechanics 44 (5) (2007) 339–346.

[36] H. H. Bui, R. Fukagawa, K. Sako, S. Ohno, Lagrangian meshfree particles method (sph) for large deformation and failure flows of geomaterial using elastic–plastic soil constitutive model, International journal for numerical and analytical methods in geomechanics 32 (12) (2008) 1537–1570.

[37] C. T. Nguyen, C. T. Nguyen, H. H. Bui, G. D. Nguyen, R. Fukagawa, A new sph-based approach to simulation of granular flows using viscous damping and stress regularisation, Landslides 14 (1) (2017) 69–81.

[38] C. Peng, X. Guo, W. Wu, Y. Wang, Unified modelling of granular media with smoothed particle hydrodynamics, Acta Geotechnica 11 (6) (2016) 1231–1247.

[39] C. Peng, S. Wang, W. Wu, H.-s. Yu, C. Wang, J.-y. Chen, Loquat: an open-source gpu-accelerated sph solver for geotechnical modeling, Acta Geotechnica 14 (5) (2019) 1269–1287.

[40] H. H. Bui, K. Sako, R. Fukagawa, J. Wells, Sph-based numerical simulations for large deformation of geomaterial considering soil-structure interaction, in: The 12th international conference of international association for computer methods and advances in geomechanics (IACMAG), Vol. 1, Citeseer, 2008, pp. 570–578.

[41] C. Peng, W. Wu, H.-s. Yu, C. Wang, A sph approach for large deformation analysis with hypoplastic constitutive model, Acta Geotechnica 10 (6) (2015) 703–717.

[42] R. Feng, G. Fourtakas, B. D. Rogers, D. Lombardi, Large deformation analysis of granular materials with stabilized and noise-free stress treatment in smoothed particle hydrodynamics (sph), Computers and Geotechnics 138 (2021) 104356.

[43] W. Hu, M. Rakhsha, L. Yang, K. Kamrin, D. Negrut, Modeling granular material dynamics and its two-way coupling with moving solid bodies using a continuum representation and the sph method, Computer Methods in Applied Mechanics and Engineering 385 (2021) 114022.

[44] J. Wang, D. Chan, Frictional contact algorithms in sph for the simulation of soil–structure interaction,

International Journal for Numerical and Analytical Methods in Geomechanics 38 (7) (2014) 747–770.

[45] L. Zhan, C. Peng, B. Zhang, W. Wu, A sph framework for dynamic interaction between soil and rigid body system with hybrid contact method, International Journal for Numerical and Analytical Methods in Geomechanics 44 (10) (2020) 1446–1471.

[46] B. Sheikh, T. Qiu, A. Ahmadipur, Comparison of sph boundary approaches in simulating frictional soil–structure interaction, Acta Geotechnica 16 (8) (2021) 2389–2408.

[47] M. Soleimani, C. Weißenfels, Numerical simulation of pile installations in a hypoplastic framework using an sph based method, Computers and Geotechnics 133 (2021) 104006.

[48] L. Zhan, C. Peng, B. Zhang, W. Wu, A stabilized tl–wc sph approach with gpu acceleration for three-dimensional fluid–structure interaction, Journal of Fluids and Structures 86 (2019) 329–353.

[49] A. J. Crespo, J. M. Domínguez, B. D. Rogers, M. Gómez-Gesteira, S. Longshaw, R. Canelas, R. Vacondio, A. Barreiro, O. García-Feal, Dualsphysics: Open-source parallel cfd solver based on smoothed particle hydrodynamics (sph), Computer Physics Communications 187 (2015) 204–216.

[50] G. Gudehus, A comprehensive constitutive equation for granular materials, Soils and foundations 36 (1) (1996) 1–12.

[51] E. Bauer, Calibration of a comprehensive hypoplastic model for granular materials, Soils and foundations 36 (1) (1996) 13–26.

[52] G.-R. Liu, M. B. Liu, Smoothed particle hydrodynamics: a meshfree particle method, World scientific, 2003.

[53] J. J. Monaghan, Sph without a tensile instability, Journal of computational physics 159 (2) (2000) 290–311.

[54] W. Dehnen, H. Aly, Improving convergence in smoothed particle hydrodynamics simulations without pairing instability, Monthly Notices of the Royal Astronomical Society 425 (2) (2012) 1068–1082.

[55] H. Wendland, Piecewise polynomial, positive definite and compactly supported radial functions of minimal degree, Advances in computational Mathematics 4 (1) (1995) 389–396.

[56] H. H. Bui, G. D. Nguyen, Smoothed particle hydrodynamics (sph) and its applications in geomechanics: From solid fracture to granular behaviour and multiphase flows in porous media, Computers and Geotechnics 138 (2021) 104315.

[57] A. English, J. Domínguez, R. Vacondio, A. Crespo, P. Stansby, S. Lind, M. Gómez-Gesteira, Correction for dynamic boundary conditions, in: Proceedings of the 14th International SPHERIC Workshop, Exeter, UK, 2019, pp. 25–27.

[58] S. Marrone, M. Antuono, A. Colagrossi, G. Colicchio, T. Le, O. García-Feal, I. Martínez-Estévez, A. Mokos, R. Vacondio, A. J. Crespo, et al., Dualsphysics: from fluid dynamics to multiphysics problems, Computational Particle Mechanics 9 (5) (2022) 867–895.

[59] S. Marrone, M. Antuono, A. Colagrossi, G. Colicchio, D. Le Touzé, G. Graziani, δ-sph model for simulating violent impact flows, Computer Methods in Applied Mechanics and Engineering 200 (13-16) (2011) 1526–1542.

[60] I. Herle, G. Gudehus, Determination of parameters of a hypoplastic constitutive model from properties of grain assemblies, Mechanics of Cohesive-frictional Materials: An International Journal on Experiments, Modelling and Computation of Materials and Structures 4 (5) (1999) 461–486.

[61] J. J. Monaghan, A. Kos, Solitary waves on a cretan beach, Journal of waterway, port, coastal, and ocean engineering 125 (3) (1999) 145–155.

[62] G. Lube, H. E. Huppert, R. S. J. Sparks, M. A. Hallworth, Axisymmetric collapses of granular columns, Journal of Fluid Mechanics 508 (2004) 175–199.

[63] H. Rezaei, C. J. Lim, A. Lau, S. Sokhansanj, Size, shape and flow characterization of ground wood chip and ground wood pellet particles, Powder Technology 301 (2016) 737–746.

[64] W. Jin, J. Klinger, T. Westover, H. Huang, A density dependent drucker-prager/cap model for ring shear simulation of ground loblolly pine, Powder Technology 368 (2020) 45–58.

[65] R. P. Schultz, Loblolly pine: the ecology and culture of the loblolly pine (Pinus taeda L.), no. 713, US Government Printing Office, 1997.

[66] L. Jordan, A. Clark, L. R. Schimleck, D. B. Hall, R. F. Daniels, Regional variation in wood specific gravity of planted loblolly pine in the united states, Canadian journal of forest research 38 (4) (2008) 698–710.

[67] J. J. Monaghan, Smoothed particle hydrodynamics and its diverse applications, Annual Review of Fluid Mechanics 44 (2012) 323–346.

[68] W. Benz, Smooth particle hydrodynamics: a review, The numerical modelling of nonlinear stellar pulsations (1990) 269–288.

[69] R. Vacondio, C. Altomare, M. De Leffe, X. Hu, D. Le Touzé, S. Lind, J.-C. Marongiu, S. Marrone, B. D. Rogers, A. Souto-Iglesias, Grand challenges for smoothed particle hydrodynamics numerical schemes, Computational Particle Mechanics 8 (3) (2021) 575–588.

[70] X. Hu, N. A. Adams, An incompressible multi-phase sph method, Journal of computational physics 227 (1) (2007) 264–278.

[71] R. Saurel, F. Petitpas, R. A. Berry, Simple and efficient relaxation methods for interfaces separating compressible fluids, cavitating flows and shocks in multiphase mixtures, journal of Computational Physics 228 (5) (2009) 1678–1712.

[72] R. Xu, P. Stansby, D. Laurence, Accuracy and stability in incompressible sph (isph) based on the projection method and a new approach, Journal of computational Physics 228 (18) (2009) 6703–6725.

[73] S. Adami, X. Hu, N. A. Adams, A transport-velocity formulation for smoothed particle hydrodynamics,

Journal of Computational Physics 241 (2013) 292–307.

[74] A. Y. Chernyshenko, M. A. Olshanskii, Y. V. Vassilevski, A hybrid finite volume–finite element method for bulk–surface coupled problems, Journal of Computational Physics 352 (2018) 516–533.